Supporting Information

In Silico Design of 2D Polymers Containing Truxene-Based Platforms: Insights into their Structural and Electronic Properties

Sergio Gámez-Valenzuela,[a] Marcelo Echeverri,[b] Berta Goḿez-Lor,[b*] José I. Martínez[b*] and M. Carmen Ruiz Delgado[a*]

[a] Dept. of Physical Chemistry, University of Málaga, Campus de Teatinos s/n, 29071, Málaga, Spain. [b] Dept. of Nanostructures and Low-dimensional Materials, Instituto de Ciencia de Materiales de Madrid (ICMM-CSIC), C/ Sor Juana Inés de la Cruz 3, Madrid 28049, Spain.

*Corresponding authors: bgl@icmm.csic.es; joseignacio.martinez@icmm.csic.es; carmenrd@uma.es

Page

S1. Theoretical Methods and Computational Details

Molecular fragments. First, molecular fragments of the 2D polymers under study (dimers for $\mathbf{T_2}$ and $\mathbf{T_3}$ and trimers for $\mathbf{T_{2,3}}$, see Figure S1) were performed in the framework of the density functional theory (DFT) using the Gaussian16 program.[1] Note that it has been recently demonstrated that calculations of molecular fragments provide important information about the molecular, electronic structure and charge-transport properties of 2D conjugated polymers.[2–9] To this end, two different hybrid functionals were used, such as the hybrid generalized gradient approximation (GGA) functional PBE0[10] and the long-range corrected hybrid functional CAM-B3LYP[11] together with the 6-31G**[12,13] and the cc-pVDZ[14] basis sets. All geometrical parameters were allowed to vary independently, and the calculated geometries were confirmed as minima by frequency calculations. The molecular orbitals were plotted using ChemCraft.[15] Interestingly, PBE0 and CAM-B3LYP functionals and the two different 6-31G** and cc-pVDZ basis sets predict the same trend in the description of the structural properties (*i.e.*, compare Fig. 2 in the main text and Fig S3 in the ESI with Fig. S4) and HOMO-LUMO gaps (*i.e.*, compare Fig. 3a in the main text with Fig. S5 in the SI) and topologies of the $\mathbf{T_2}$ an $\mathbf{T_3}$ dimeric models (*i.e.*, compare Fig. 3b in the main text and Fig. S6 with Fig. S7 in the SI).

NICS methodology. The NICS[16,17] values were calculated at the CAM-B3LYP/6-311++G(2df,p) level from the CAM-B3LYP/cc-pVDZ optimized structures by using the gauge-independent atomic orbital (GIAO)[18] method.

Intramolecular reorganization energies. We also carried out optimizations of the radical-ion states associated with the model dimers in order to analyze the intramolecular reorganization energies for holes (λ_h) and electron transfer (λ_e). The λ values were calculated directly from the relevant points on the potential energy surfaces by means of a standard procedure reported in the literature.[19,20]

Periodic calculations. In a step forward, we used periodic boundary conditions to obtain the geometry optimizations of 2D COF structures of all polymers under study. For that purpose, the preliminary optimized building blocks (at CAM-B3LYP/cc-pVDZ level) can be considered reasonable starting point geometries towards the assembling of the whole COF systems. Once the 2D COFs were constructed, they were fully optimized (simultaneous lattice/cell and structure optimizations) with the QUANTUM EXPRESSO plane- wave DFT code.[21] Within this implementation, the GGA-PBE[22] functional was used to account for the exchange-correlation (XC) effects, at the same time that we use the Grimme DFT-D3 semi-empirical efficient vdW correction to include dispersion forces and energies in conventional DFT functionals.[23] Ultra-soft pseudopotentials have been used to model the ion-electron interaction within the C, N, O and H atoms.[24,25] The Brillouin zones have been sampled by means of optimal Monkhorst-Pack grids.[26] In this regard, the one-electron wave-functions are expanded in a basis of plane-waves with a kinetic energy cutoff of 41 Ry for the kinetic energy and 260 Ry for electronic density. The energy cutoff values have been tested to achieve sufficient accuracy to guarantee a full convergence in total energy and electronic density. As mentioned, we have performed simultaneous full lattice/cell and structure optimizations for all the different periodic 2D systems. The atomic relaxations were carried out within a conjugate gradient minimization scheme until the maximum force acting on any atom was below 0.02 eV Å^{-}

[1]. Relaxations of cell shape and size have been double-checked with two different algorithms:a damped dynamics, and a Broyden–Fletcher–Goldfarb–Shanno-like relaxation.[27–29] These two approaches, tested thoroughly in the literature for different crystal bulk and molecular configurations, provide very similar and satisfactory results for cell-shape and lattice parameters.
Inter-layer distances have been fully-relaxed following the afore mentioned simultaneous lattice+structure relaxation protocol. Inter-layer cohesive energies for the crystal-bulks analyzed in the study have been obtained in their both AA and AB stacking fashions as the difference between the total energies of the crystal bulks (with one layer per unit cell) and the optimized corresponding single-layers.

Topologies of valence and conduction bands. 3D isosurfaces of the orbital electronic densities corresponding to the valence and conduction electronic states of the different extended 2D COF systems studied here ($||\Psi_{cond}(\mathbf{r})||^2$ and $||\Psi_{val}(\mathbf{r})||^2$) at the k-point corresponding to the direct band gap have been plotted using the the VMD 1.9.3 program.[30] The same program has been used in order to represent the surface charge distributions of the resulting 2D COFs. From these figures we can extract information about the spatial localization and delocalization degree of these states, which may directly connect with the transport performance of the systems, the homogeneity in the spatial distribution of the states, which is related to the spatial coherence of the electronic properties, as well as the preferential carrier transport paths across the compounds. All of them have been depicted with the same isosurface value (0.0003 e^-/A) for sake of comparison between them.

UV-Vis spectra. Photoexcitation (optical absorption) spectra of the periodic layers have been computed by the Time-dependent DFT formalism as implemented in the QUANTUM ESPRESSO simulation package.[31,32] Within this theoretical framework the excitation spectrum is obtained as:

$$I(\omega) \propto Im[\bar{\alpha}(\omega)], \qquad \text{eq. (3)}$$

where $I(\omega)$ is the absorption intensity, and $Im[\bar{\alpha}(\omega)]$ is the imaginary part of $\bar{\alpha}(\omega)$, the averaged (average of the diagonal elements) dipole polarizability. This dynamical polarizability is represented in terms of the resolvent of its Liouvillian super-operator within TD-DFT, and evaluated using a non-Hermitean Lanczos method, whose implementation does not require the calculation of virtual states.[31,32]

Effective masses. Effective hole and electron masses, m^*_h and m^*_e, have been evaluated for the top of the valence band and the bottom of the conduction band, respectively, for those systems with a significant electronic band dispersion via the following expression:

$$m^* = \hbar^2 \left\{ \frac{\partial^2 E}{\partial k^2} \right\}^{-1}, \qquad \text{eq. (4)}$$

The *E(k)* function has been parametrized and fitted by a quadratic anharmonical expression $E(k) = a_0 + a_1 \times k + a_2 \times k^2$ within a close region to the band-gap k-point, with the rest of quantities in atomic units to obtain the effective masses directly in m_e units.

S2. Study of Molecular Fragments

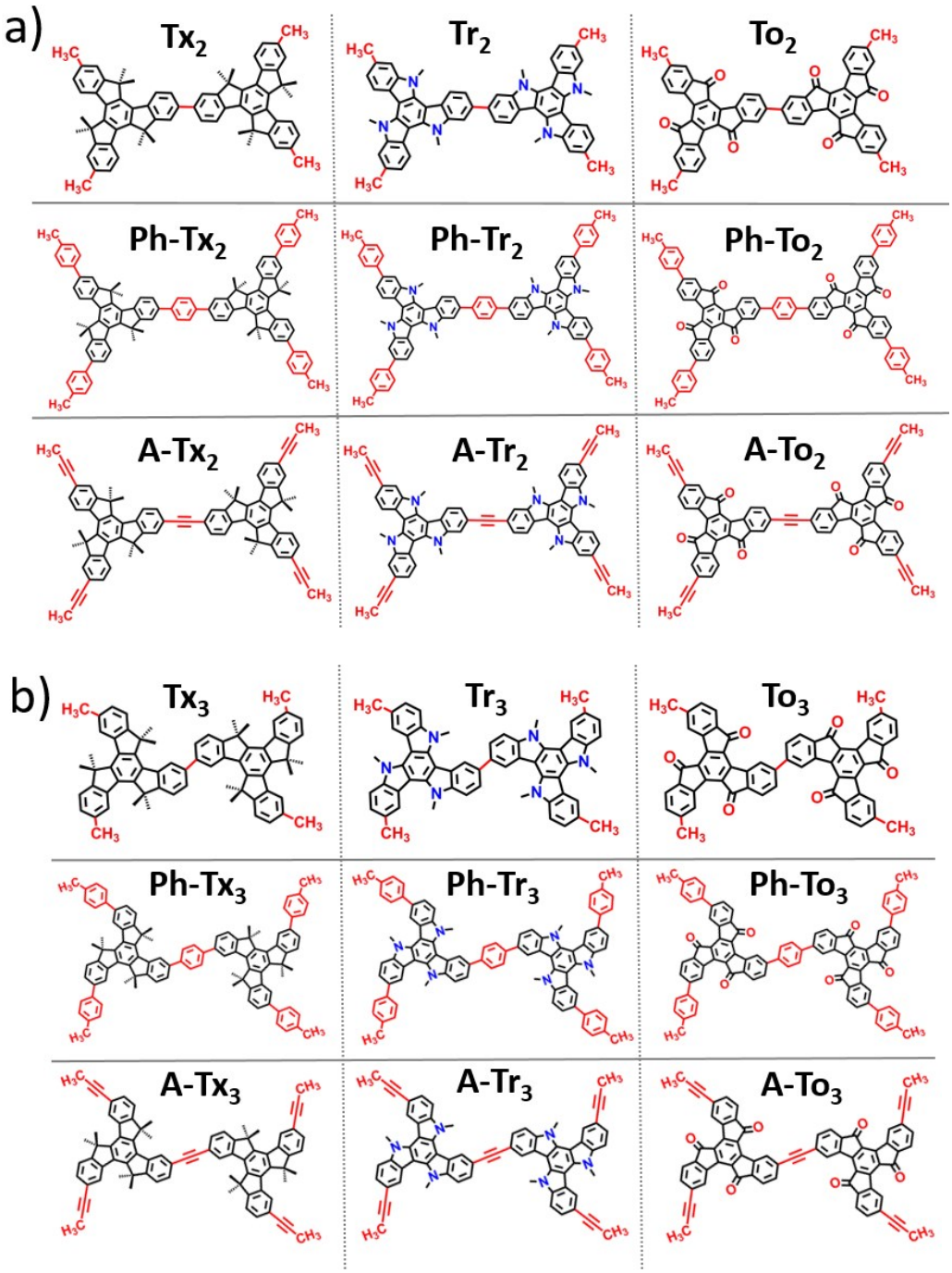

Figure S1. Chemical structures of $\mathbf{T_2}$ (a) and $\mathbf{T_3}$ (b) dimeric models studied theoretically.

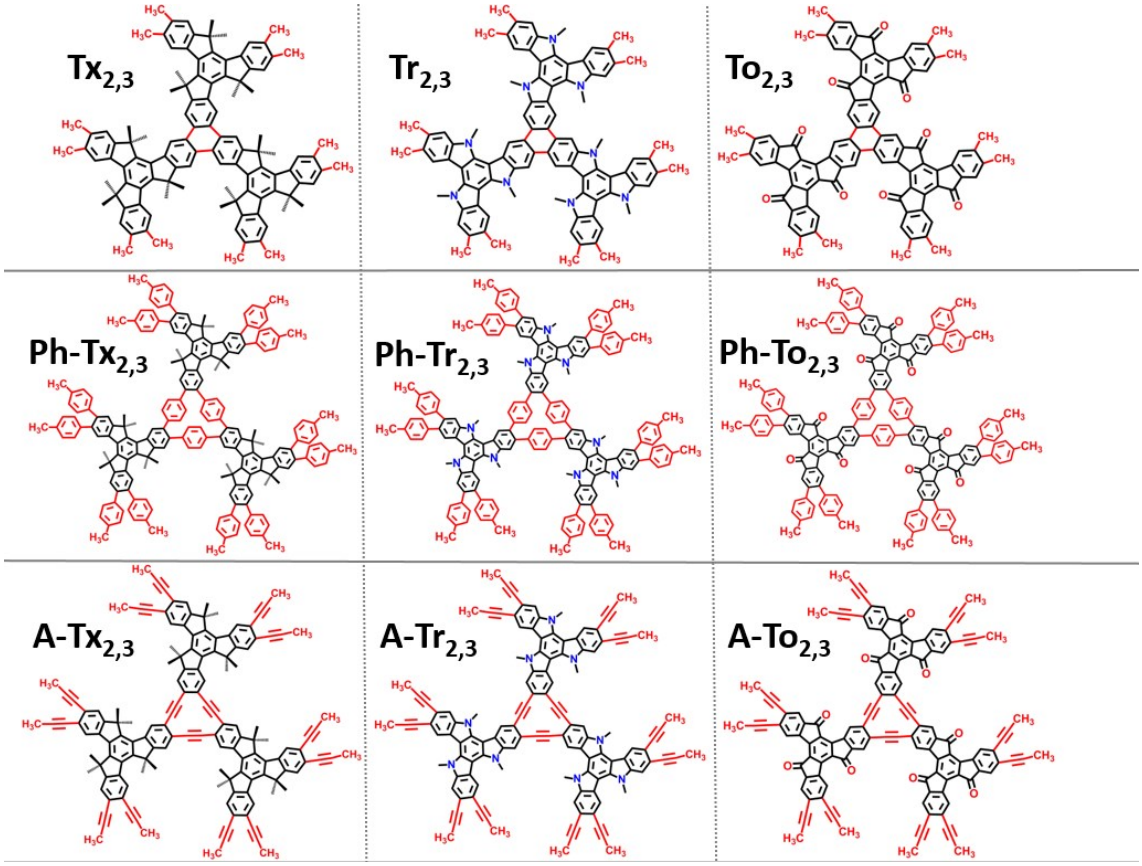

Figure S2. Chemical structures of $\mathbf{T_{2,3}}$ trimeric models studied theoretically.

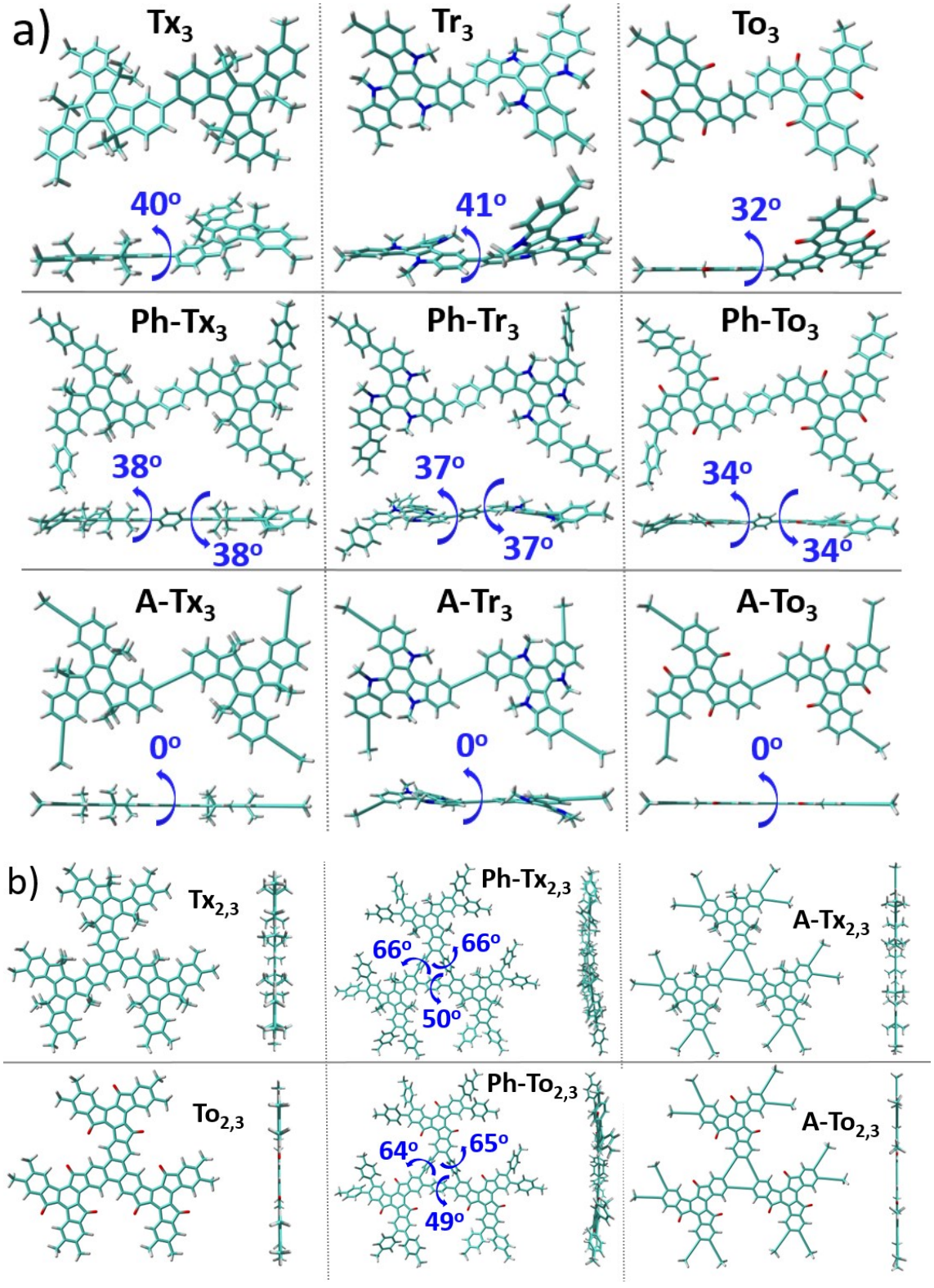

Figure S3. Top and lateral views of the DFT-optimized structures (PBE0/6-31G** level) for (a) $\mathbf{T_3}$ dimeric models and (b) $\mathbf{Tx_{2,3}}$ and $\mathbf{To_{2,3}}$ trimeric models. The dihedral angles between the conjugated cores and the π-bridges (in absolute values) are also shown.

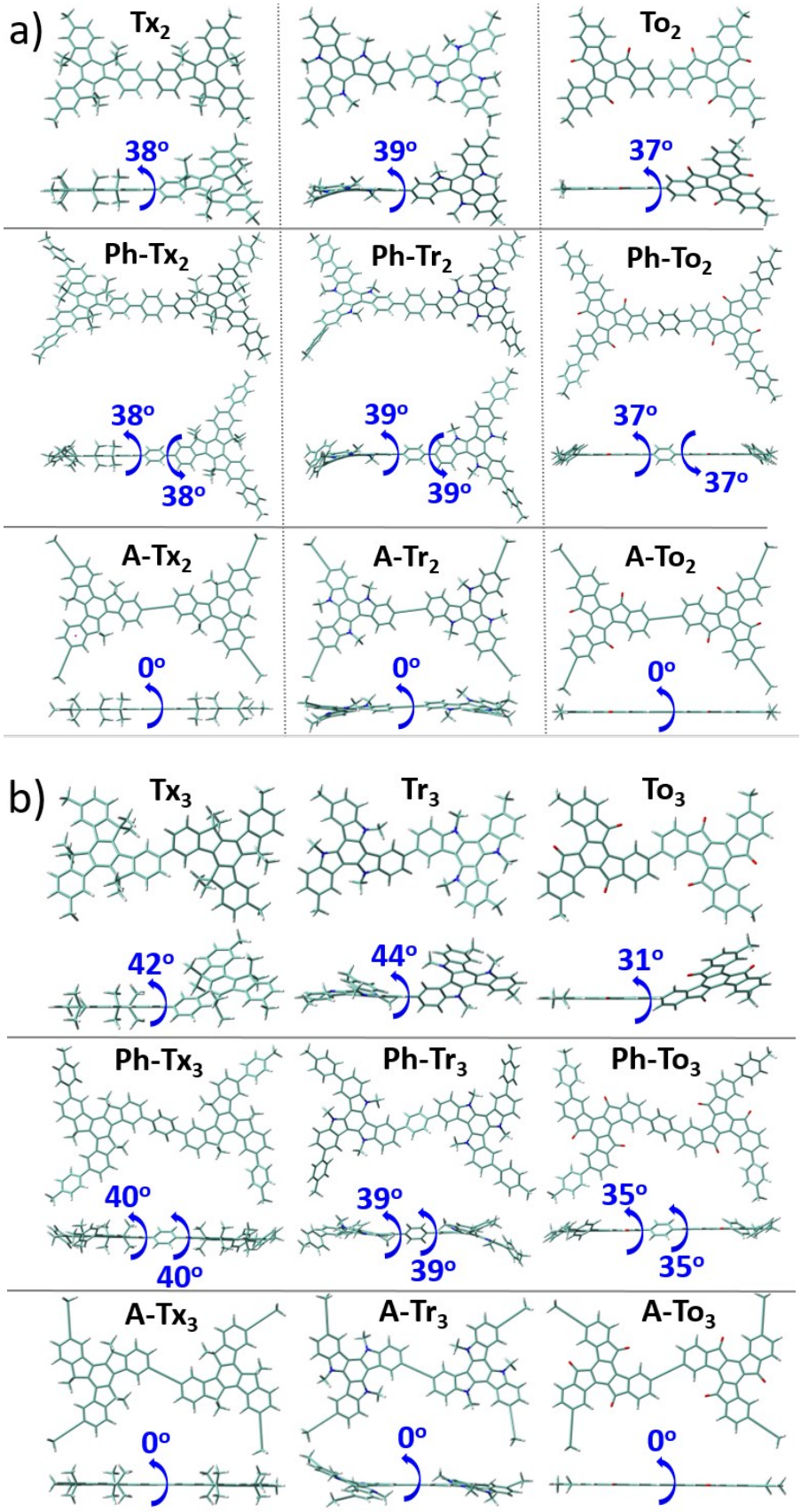

Figure S4. Top and lateral views of the DFT-optimized structures (CAM-B3LYP/cc-pVDZ level) for (a) $\mathbf{T_2}$ and (b) $\mathbf{T_3}$ dimeric models. The dihedral angles between the conjugated cores and the π-bridges (in absolute values) are also shown.

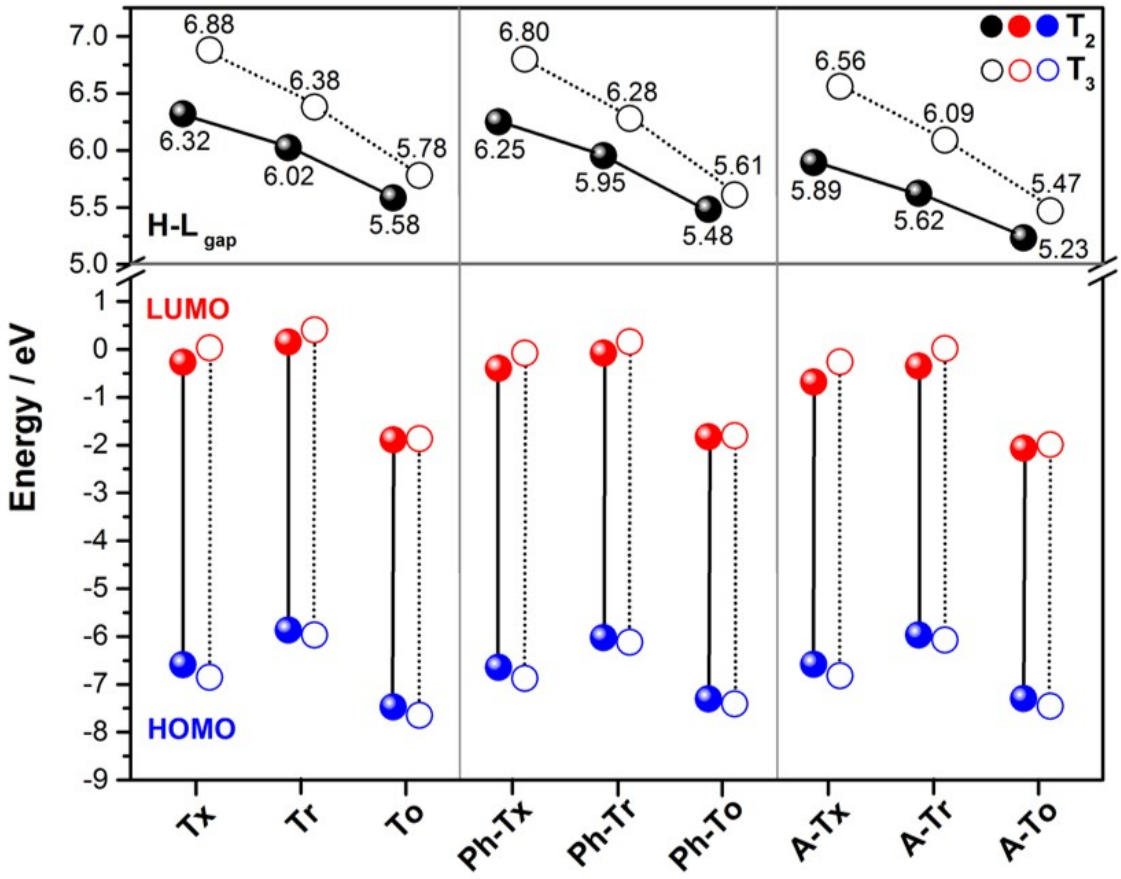

Figure S5. DFT-calculated (CAM-B3LYP/cc-pVDZ level) HOMO-LUMO gap (top) and frontier molecular orbital energies (bottom) for (a) $\mathbf{T_2}$ (solid circles) and $\mathbf{T_3}$ (open circles) dimeric models.

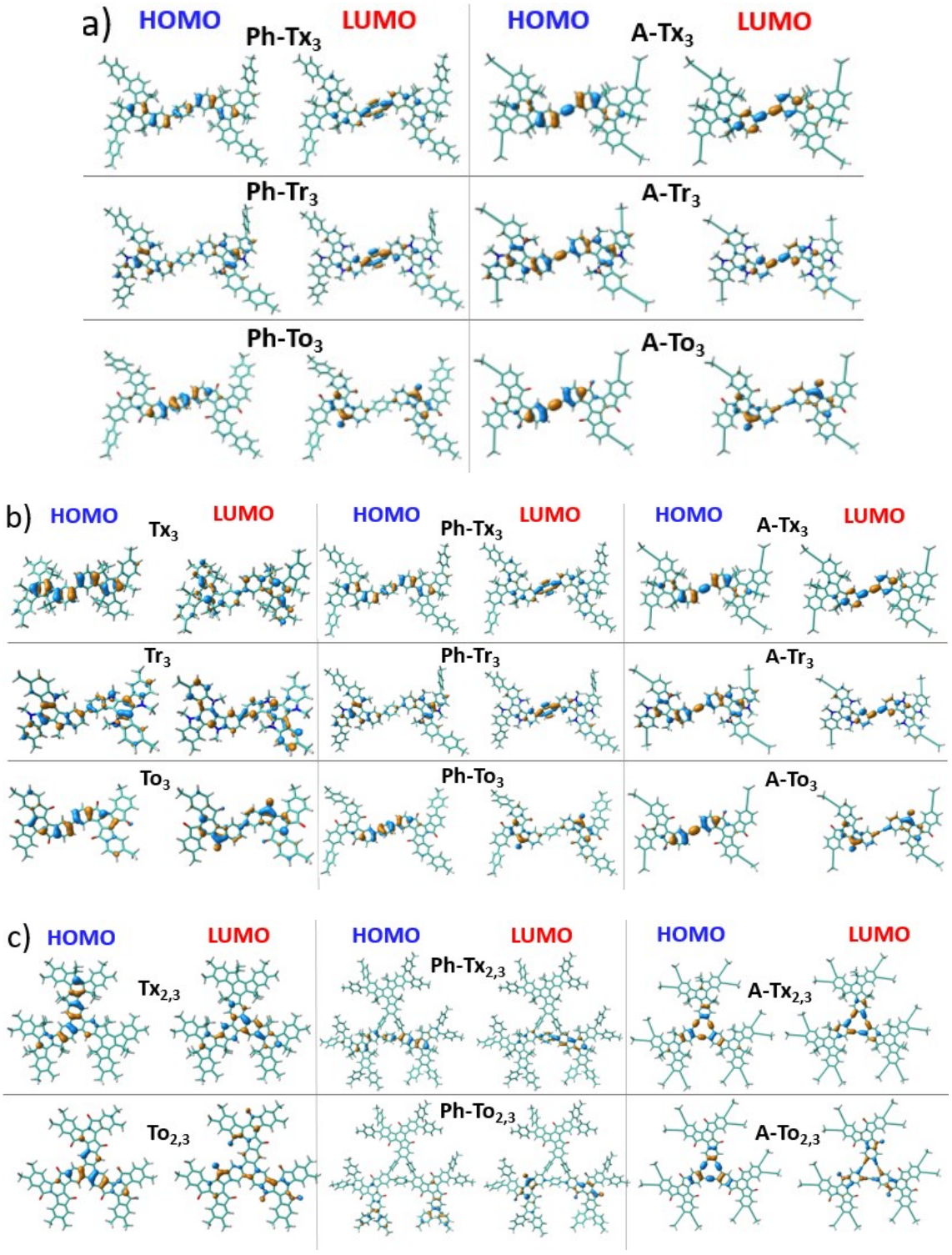

Figure S6. DFT-calculated (PBE0/6-31G** level) HOMO and LUMO topologies of (a) **Ph-T$_2$** and **A-T$_2$** dimeric models, (b) **T$_3$** dimeric models and (c) **Tx$_{2,3}$** and **To$_{2,3}$** trimeric models.

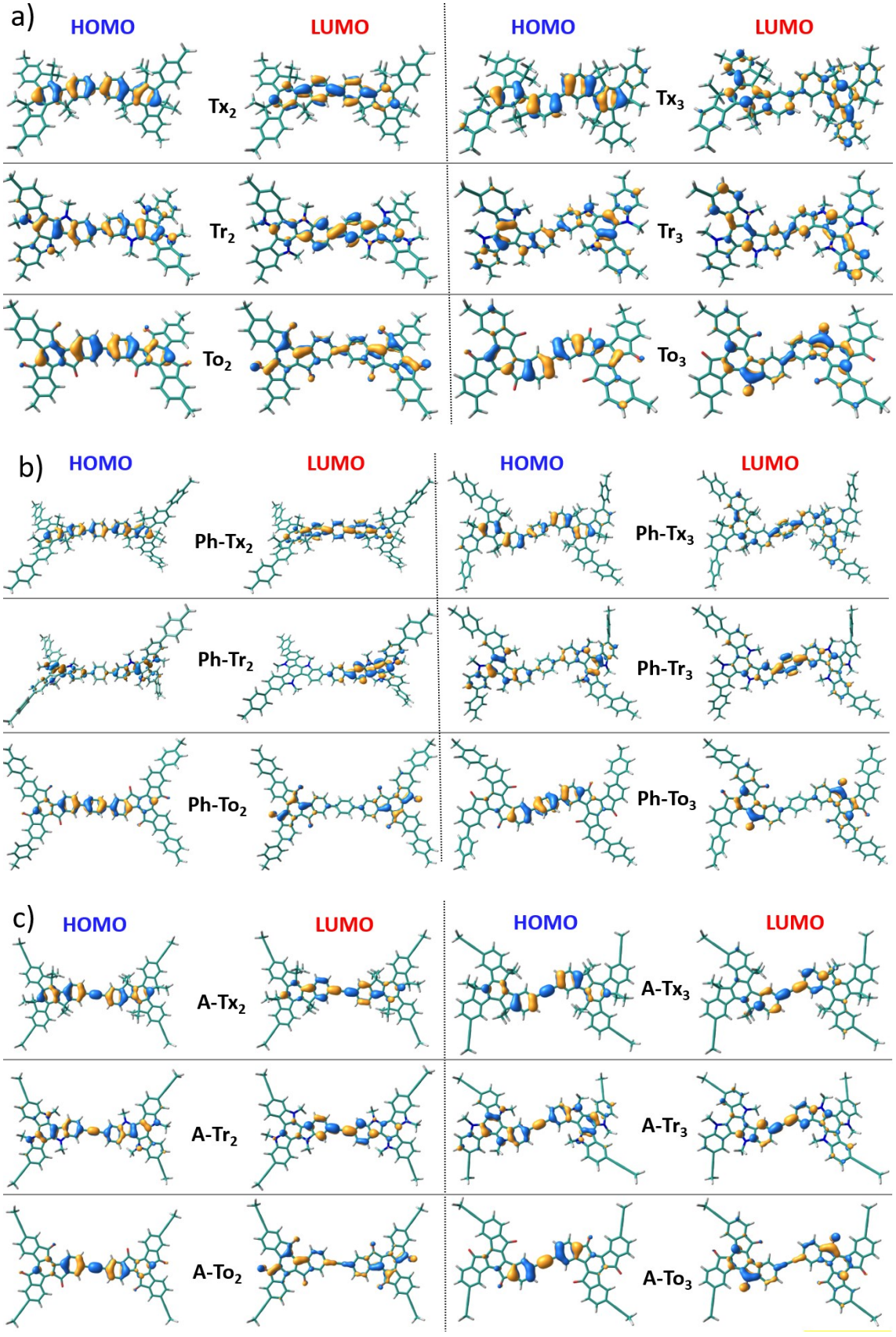

Figure S7. DFT-calculated (CAM-B3LYP/cc-pVDZ level) HOMO and LUMO topologies of (a) directly covalently linked, (b) phenylene-substituted and (c) alkyne-substituted $\mathbf{T_2}$ and $\mathbf{T_3}$ dimeric models.

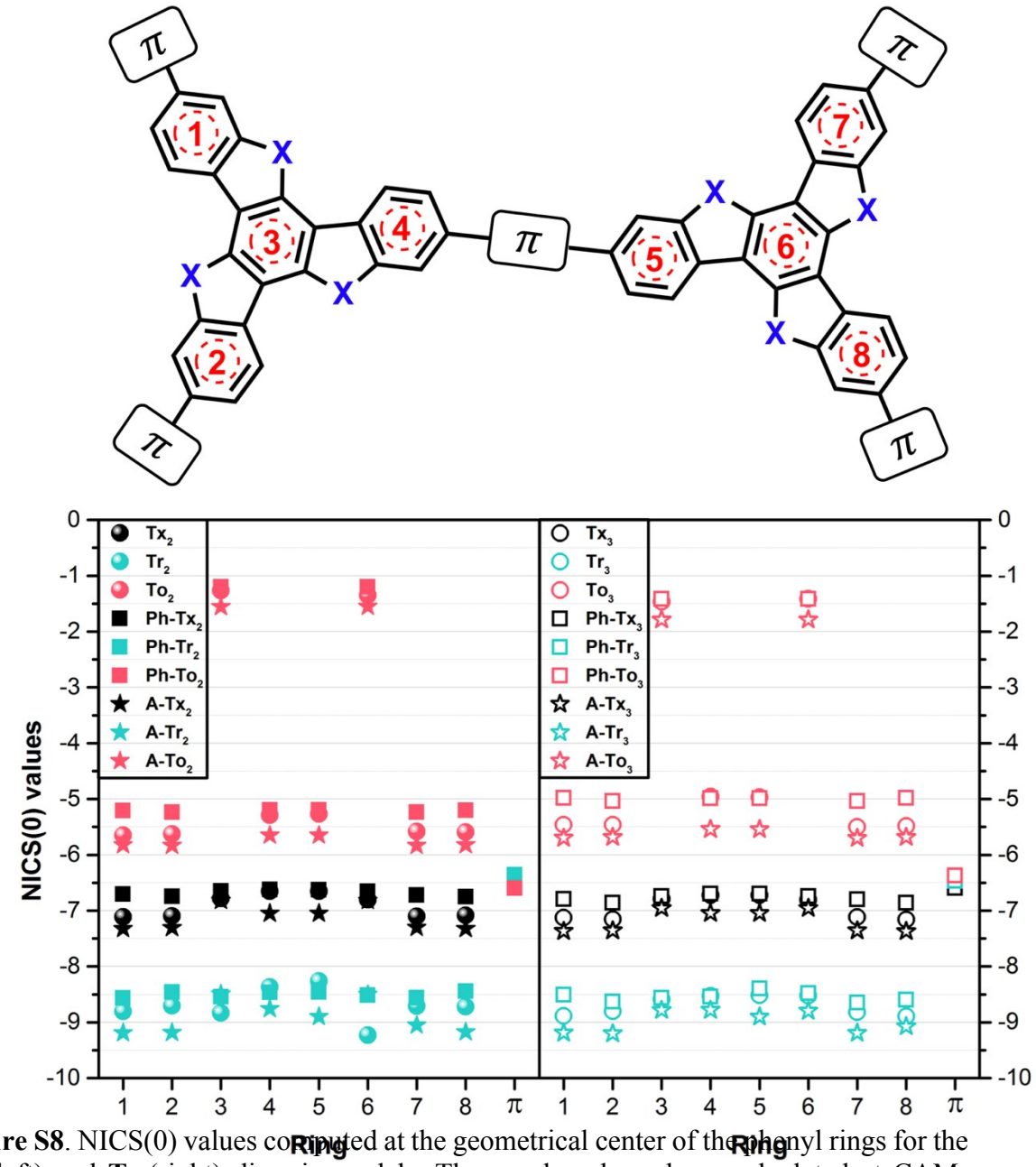

Figure S8. NICS(0) values computed at the geometrical center of the phenyl rings for the $\mathbf{T_2}$ (left) and $\mathbf{T_3}$ (right) dimeric models. These values have been calculated at CAM-B3LYP/6-311++G(2df,p)//CAM-B3LYP/cc-pVDZ level of theory and they are given in ppm.

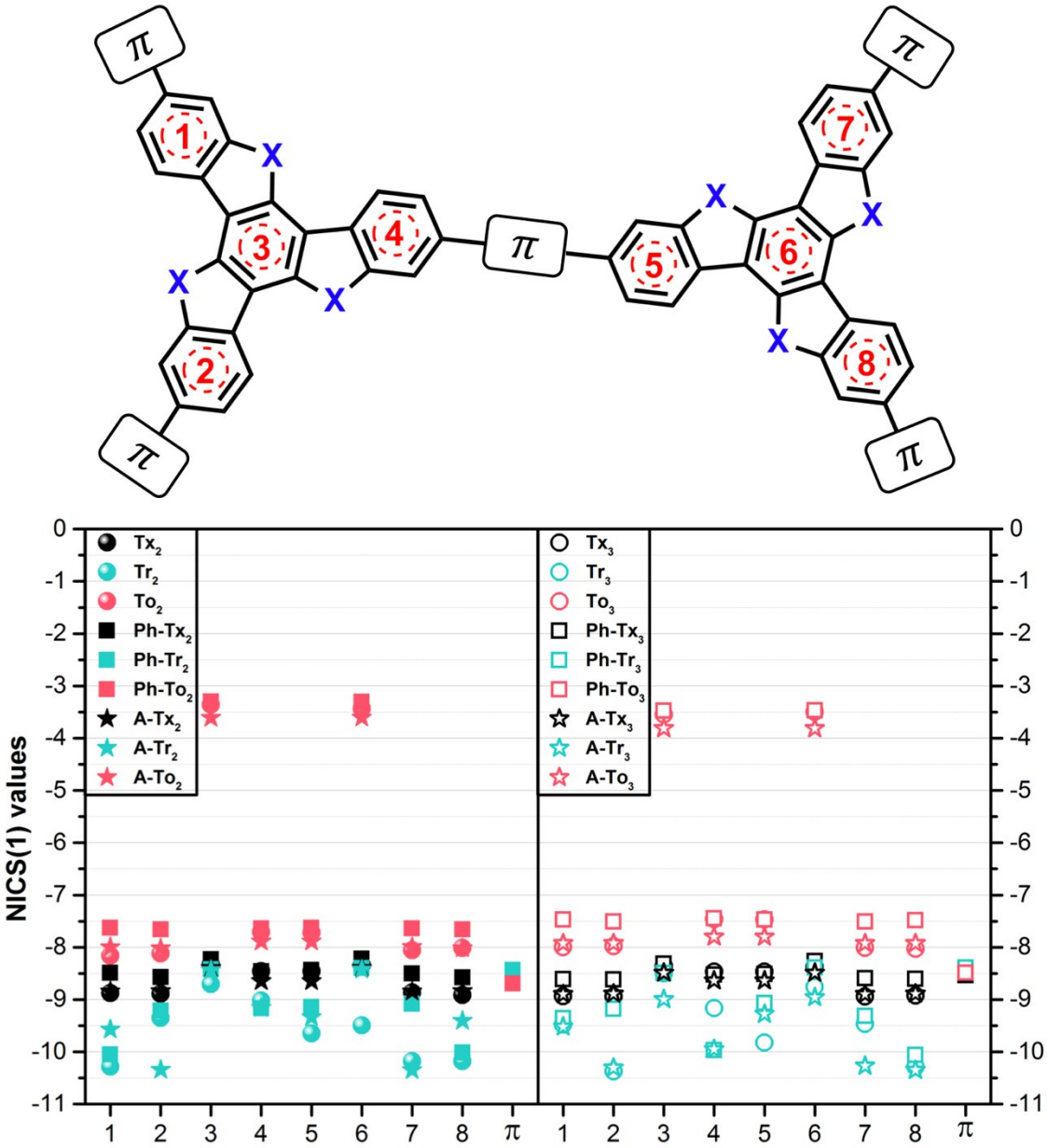

Figure S9. NICS(1) values computed at the geometrical center of the phenyl rings for the $\mathbf{T_2}$ (left) and $\mathbf{T_3}$ (right) dimeric models. These values have been calculated at CAM-B3LYP/6-311++G(2df,p)//CAM-B3LYP/cc-pVDZ level of theory and they are given in ppm.

S3. Study of 2D Conjugated Polymer Networks

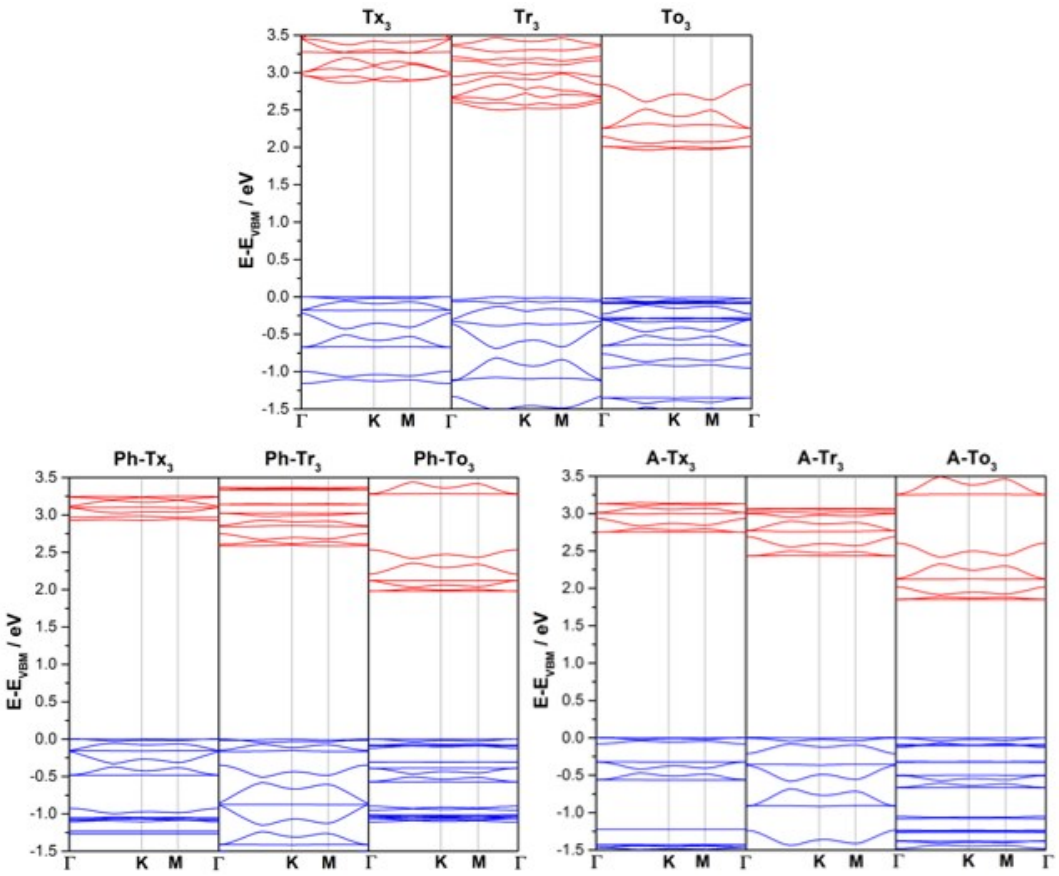

Figure S10. DFT-PBE-calculated electronic band structures of **Tx$_3$**, **Tr$_3$** and **To$_3$** (top), **Ph-Tx$_3$**, **Ph-Tr$_3$** and **Ph-To$_3$** (bottom, left) and **A-Tx$_3$**, **A-Tr$_3$**,and **A-To$_3$** (bottom, right) 2D-COFs. The valence and conduction bands are marked in blue and red, respectively. The zero energy is taken to correspond to the valence band maximum, E_{VBM}, while the x-axis labels denote a path through the 3D space of k-vectors. Points of high symmetry in the Brillouin zone are labeled as **Γ**(0, 0, 0), **M**(0, 1/2, 0) and **K**(1/3, 2/3, 0), all in reciprocal space crystal coordinates.

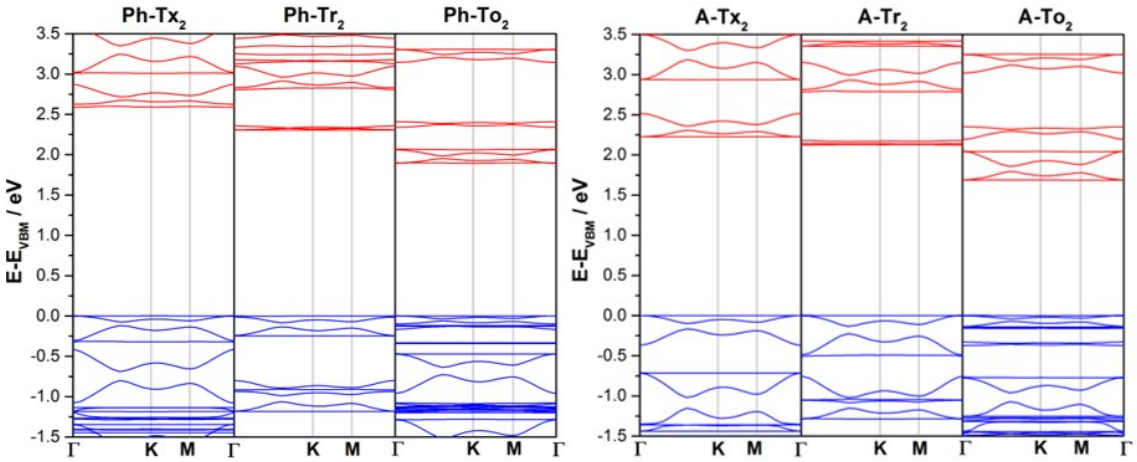

Figure S11. DFT-PBE-calculated electronic band structures of **Ph-Tx$_2$**, **Ph-Tr$_2$** and **Ph-To$_2$** (left) and **A-Tx$_2$**, **A-Tr$_2$** and **A-To$_2$** (right) 2D-COFs. The valence and conduction bands are marked in blue and red, respectively. The zero energy is taken to correspond to the valence band maximum, E_{VBM}, while the x-axis labels denote a path through the 3D space of k-vectors. Points of high symmetry in the Brillouin zone are labeled as **Γ**(0, 0, 0), **M**(0, 1/2, 0) and **K**(1/3, 2/3, 0), all in reciprocal space crystal coordinates.

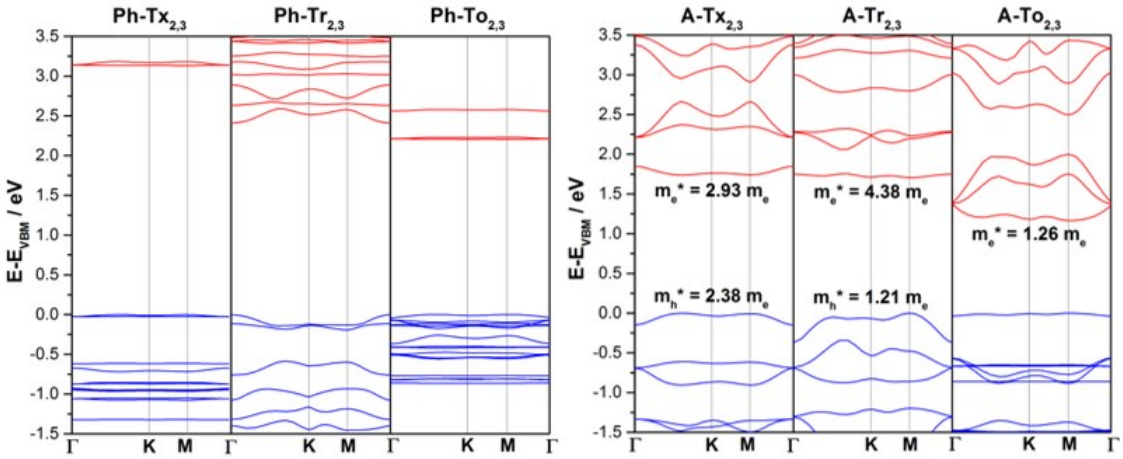

Figure S12. DFT-PBE-calculated electronic band structures of **Ph-Tx$_{2,3}$**, **Ph-Tr$_{2,3}$** and **Ph-To$_{2,3}$** (left) and **A-Tx$_{2,3}$**, **A-Tr$_{2,3}$** and **A-To$_{2,3}$** (right) 2D-COFs. The valence and

conduction bands are marked in blue and red, respectively. The zero energy is taken to correspond to the valence band maximum, E_{VBM}, while the x-axis labels denote a path through the 3D space of k-vectors. Points of high symmetry in the Brillouin zone are labeled as **Γ**(0, 0, 0), **M**(0, 1/2, 0) and **K**(1/3, 2/3, 0), all in reciprocal space crystal coordinates.

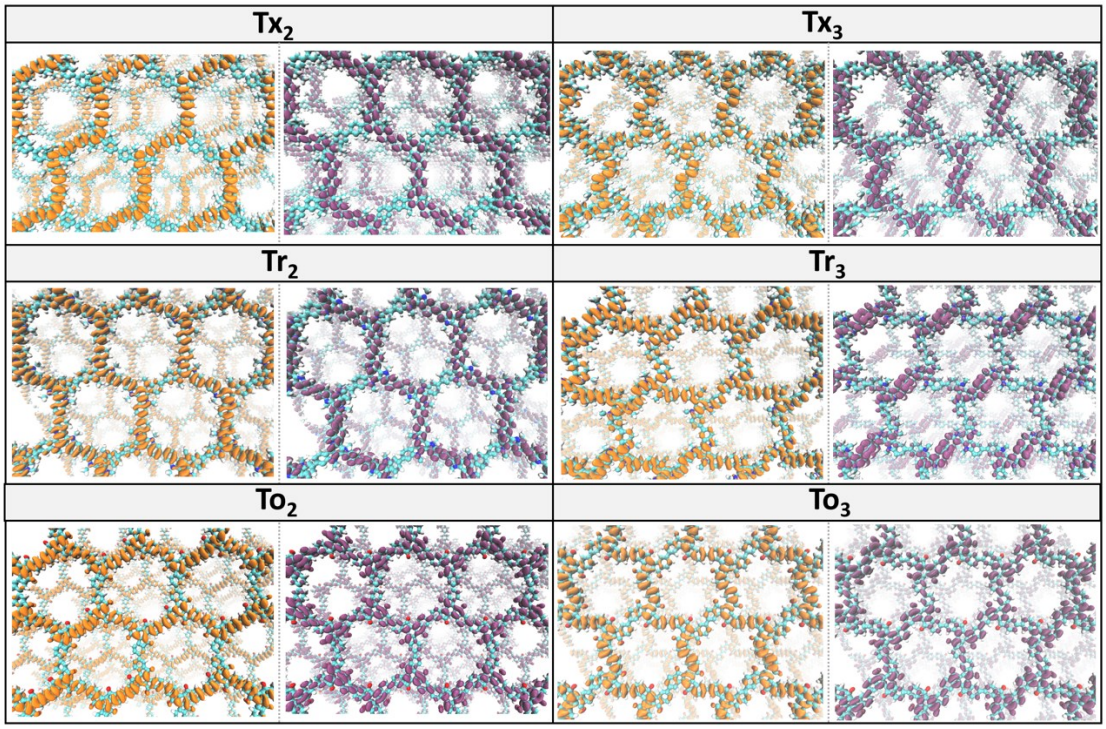

Figure S13. DFT-PBE-calculated topologies of the valence (orange) and conduction (purple) bands for directly connected **Tx-**, **Tr-** and **To**-based 2D COFs.

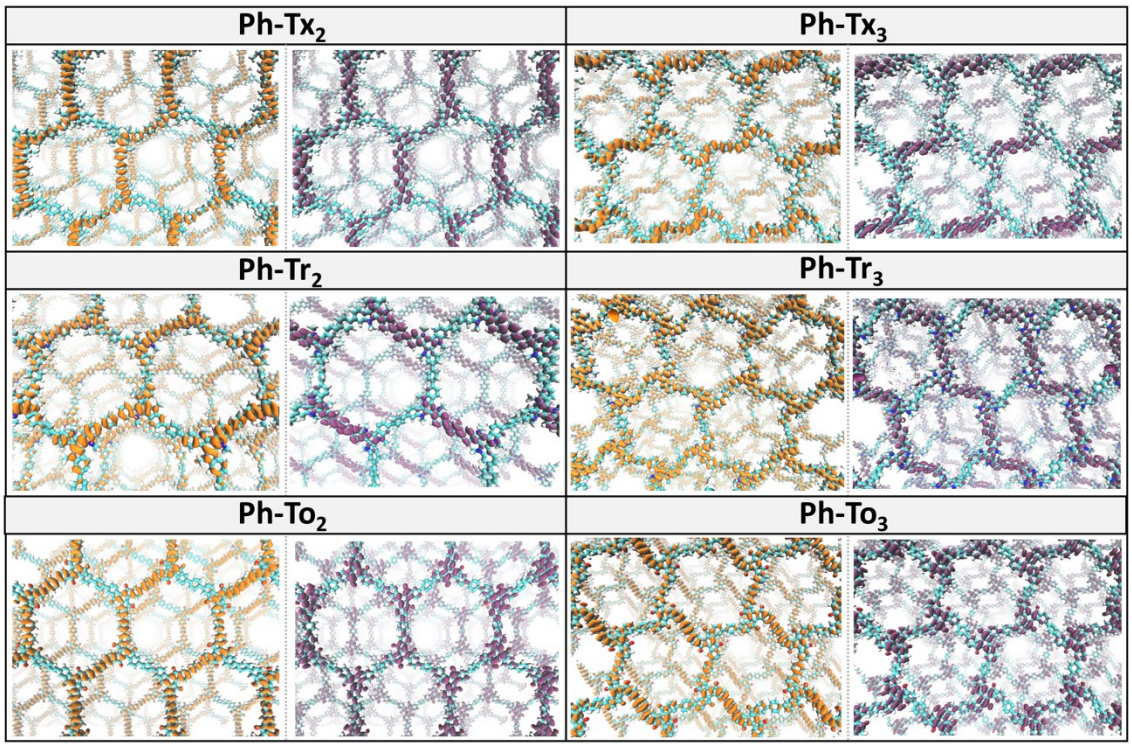

Figure S14. DFT-PBE-calculated topologies of the valence (orange) and conduction (purple) bands for phenylene-linked **Ph-Tx**, **Ph-Tr** and **Ph-To** 2D COFs.

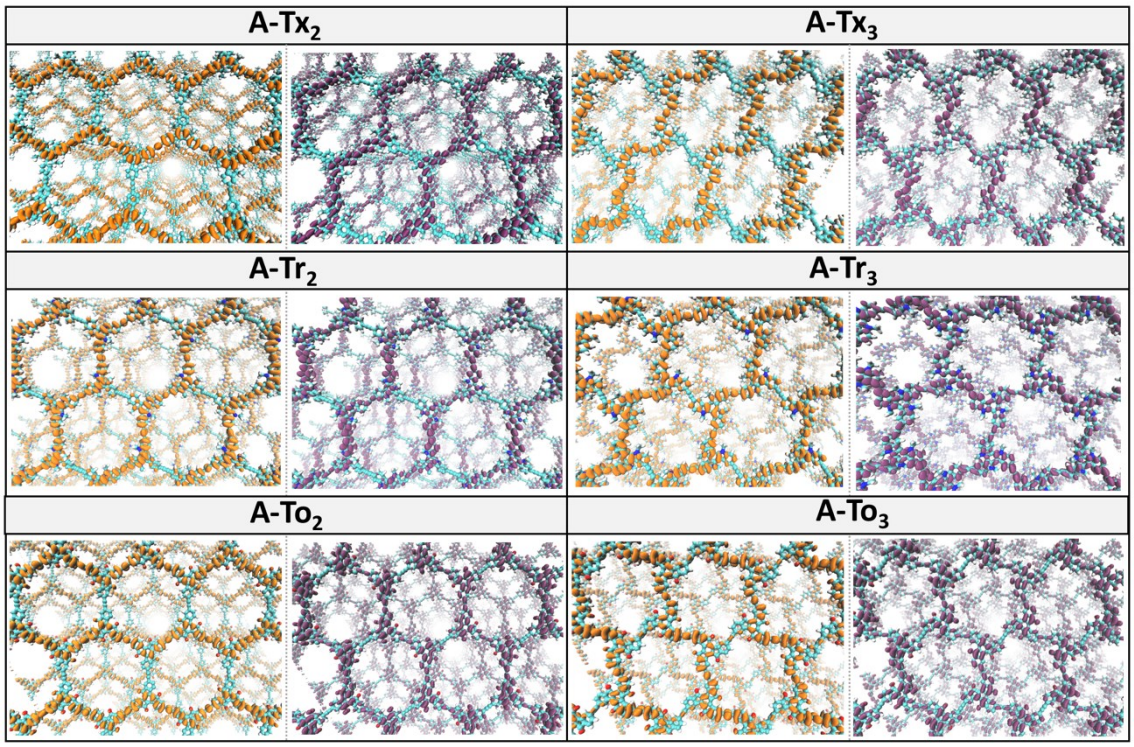

Figure S15. DFT-PBE-calculated topologies of the valence (orange) and conduction (purple) bands for alkyne-linked **A-Tx**, **A-Tr** and **A-To** 2D COFs.

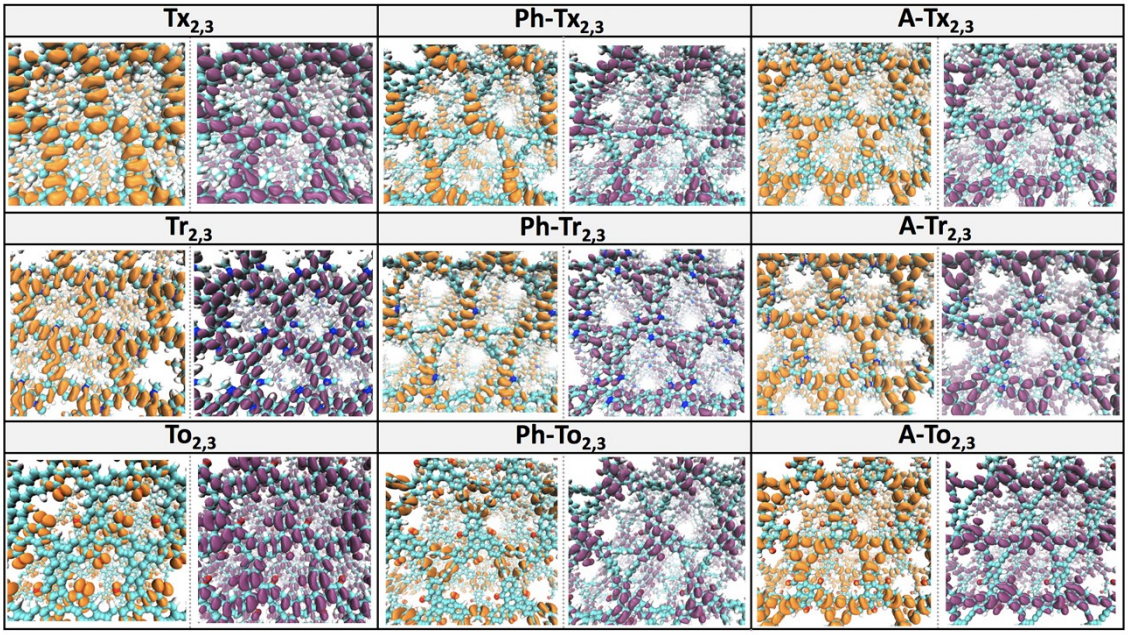

Figure S16. DFT-PBE-calculated topologies of the valence (orange) and conduction (purple) bands for $\mathbf{T_{2,3}}$ 2D COFs.

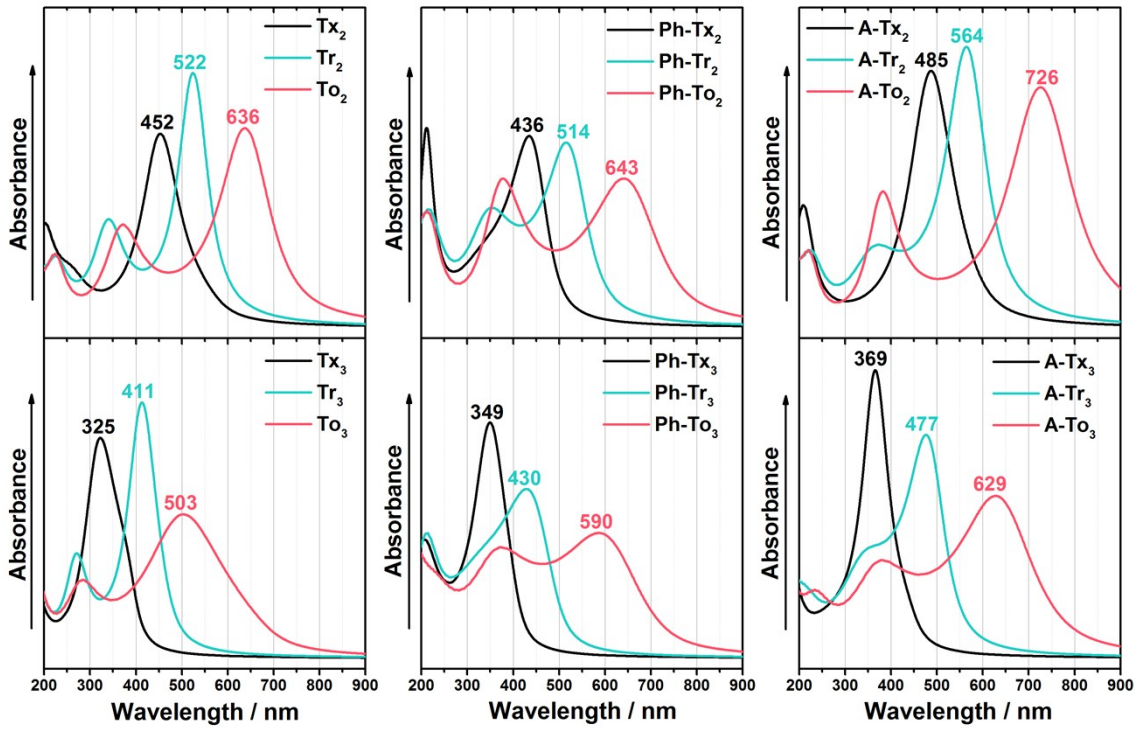

Figure S17. TD-DFT-PBE-calculated UV-Vis absorption spectra for the **Tx-** (black lines), **Tr-** (green lines) and **To**-based (red lines) $\mathbf{T_2}$ and $\mathbf{T_3}$ 2D COFs under study.

Discussion on the TD-DFT calculations for the **T_2** and **T_3** 2D COFs

The calculated spectra shown in Figure S17 are dominated by an intense band at lower energies, which corresponds to a $S_0 \rightarrow S_1$ transition assigned to one-electron promotion from the valence to the conduction band. An examination of the electronic absorption spectrum of **Tr_2** shows a strongly red-shifted band maximum (70 nm) when compared to those of **Tx_2**, being this effect even more important in the case of their **To_2** analogue (114 nm). This effect can be explained by a decrease in the band gap which is mainly ascribed to the stabilization of the conduction band minimum (CBM) in the following order: **Tx** > **Tr** > **To**. The conduction band wave functions of these compounds spread over one preferential direction along the conjugated framework, with higher contributions over other directions in **To_2**, resulting in an extension of the π-conjugation (see Figure S13). Interestingly, the electronic absorption band is red-shifted when the conjugated platforms are linked through phenylene or alkyne spacers; bathochromic shifts of 49 and 78 nm (79 and 162 nm) are observed for **Ph-Tr_2** (**A-Tr_2**) and **Ph-To_2** (**A-To_2**) respectively, in comparison with their directly linked analogues. The stronger effect played by the alkyne group can be explained by the higher planarity of alkyne-based COFs as compared to the moderately distorted phenylene-linked COFs , which facilities the extension of the π-conjugation over the whole framework allowing for large π-electron delocalization. On the other hand, the linkage position has a moderate influence on the optoelectronic properties of these 2D polymers. As a general trend, when the conjugated platforms are connected through *para* positions (**T_2** polymers), the absorption spectra are notably red-shifted when compared with those connected through *meta* positions (**T_3** polymers).

S4. References

1 M. J. Frisch, G. W. Trucks, H. B. Schlegel, G. E. Scuseria, M. a. Robb, J. R. Cheeseman, G. Scalmani, V. Barone, G. a. Petersson, H. Nakatsuji, X. Li, M. Caricato, a. V. Marenich, J. Bloino, B. G. Janesko, R. Gomperts, B. Mennucci, H. P. Hratchian, J. V. Ortiz, a. F. Izmaylov, J. L. Sonnenberg, Williams, F. Ding, F. Lipparini, F. Egidi, J. Goings, B. Peng, A. Petrone, T. Henderson, D. Ranasinghe, V. G. Zakrzewski, J. Gao, N. Rega, G. Zheng, W. Liang, M. Hada, M. Ehara, K. Toyota, R. Fukuda, J. Hasegawa, M. Ishida, T. Nakajima, Y. Honda, O. Kitao, H. Nakai, T. Vreven, K. Throssell, J. a. Montgomery Jr., J. E. Peralta, F. Ogliaro, M. J. Bearpark, J. J. Heyd, E. N. Brothers, K. N. Kudin, V. N. Staroverov, T. a. Keith, R. Kobayashi, J. Normand, K. Raghavachari, a. P. Rendell, J. C. Burant, S. S. Iyengar, J. Tomasi, M. Cossi, J. M. Millam, M. Klene, C. Adamo, R. Cammi, J. W. Ochterski, R. L. Martin, K. Morokuma, O. Farkas, J. B. Foresman and D. J. Fox, 2016, Gaussian 16, Revision C.01, Gaussian, Inc., Wallin.

2 S. Royuela, E. Martínez-Periñán, M. P. Arrieta, J. I. Martínez, M. M. Ramos, F. Zamora, E. Lorenzo and J. L. Segura, *Chem. Commun.*, 2020, **56**, 1267–1270.

3 P. Albacete, J. I. Martínez, X. Li, A. López-Moreno, S. Mena-Hernando, A. E. Platero-Prats, C. Montoro, K. P. Loh, E. M. Pérez and F. Zamora, *J. Am. Chem. Soc.*, 2018, **140**, 12922–12929.

4 L. Li, Z. Cai, Q. Wu, W. Y. Lo, N. Zhang, L. X. Chen and L. Yu, *J. Am. Chem. Soc.*, 2016, **138**, 7681–7686.

5 L. Li, W. Y. Lo, Z. Cai, N. Zhang and L. Yu, *Macromolecules*, 2016, **49**, 6903–

6909.
6 J. Wen, D. Luo, L. Cheng, K. Zhao and H. Ma, *Macromolecules*, 2016, **49**, 1305–1312.
7 R. Gutzler and D. F. Perepichka, *J. Am. Chem. Soc.*, 2013, **135**, 16585–16594.
8 S. Thomas, H. Li, R. R. Dasari, A. M. Evans, I. Castano, T. G. Allen, O. G. Reid, G. Rumbles, W. R. Dichtel, N. C. Gianneschi, S. R. Marder, V. Coropceanu and J. L. Brédas, *Mater. Horizons*, 2019, **6**, 1868–1876.
9 G. V. Baryshnikov, B. F. Minaev, N. N. Karaush and V. A. Minaeva, *RSC Adv.*, 2014, **4**, 25843–25851.
10 J. P. Perdew, M. Ernzerhof and K. Burke, *J. Chem. Phys.*, 1996, **105**, 9982–9985.
11 T. Yanai, D. P. Tew and N. C. Handy, *Chem. Phys. Lett.*, 2004, **393**, 51–57.
12 W. J. Hehre, K. Ditchfield and J. A. Pople, *J. Chem. Phys.*, 1972, **56**, 2257–2261.
13 M. M. Francl, W. J. Pietro, W. J. Hehre, J. S. Binkley, M. S. Gordon, D. J. DeFrees and J. A. Pople, *J. Chem. Phys.*, 1982, **77**, 3654–3665.
14 T. H. Dunning, *J. Chem. Phys.*, 1989, **90**, 1007–1023.
15 J. Oliver, *Hilos Tensados*, 2019, 1, 1–476.
16 P. V. R. Schleyer, C. Maerker, A. Dransfeld, H. Jiao and N. J. R. Van Eikema Hommes, *J. Am. Chem. Soc.*, 1996, **118**, 6317–6318.
17 T. K. Zywietz, H. Jiao, P. V. R. Schleyer and A. De Meijere, *J. Org. Chem.*, 1998, **63**, 3417–3422.
18 K. Wolinski, J. F. Hinton and P. Pulay, *J. Am. Chem. Soc.*, 1990, **112**, 8251–8260.
19 J. L. Brédas, D. Beljonne, V. Coropceanu and J. Cornil, *Chem. Rev.*, 2004, **104**, 4971–5003.
20 V. Coropceanu, J. Cornil, D. A. da Silva Filho, Y. Olivier, R. Silbey and J. L. Brédas, *Chem. Rev.*, 2007, 107, 926–952.
21 P. Giannozzi, S. Baroni, N. Bonini, M. Calandra, R. Car, C. Cavazzoni, D. Ceresoli, G. L. Chiarotti, M. Cococcioni, I. Dabo, A. Dal Corso, S. De Gironcoli, S. Fabris, G. Fratesi, R. Gebauer, U. Gerstmann, C. Gougoussis, A. Kokalj, M. Lazzeri, L. Martin-Samos, N. Marzari, F. Mauri, R. Mazzarello, S. Paolini, A. Pasquarello, L. Paulatto, C. Sbraccia, S. Scandolo, G. Sclauzero, A. P. Seitsonen, A. Smogunov, P. Umari and R. M. Wentzcovitch, *J. Phys. Condens. Matter*, 2009, **21**, 395502.
22 J. P. Perdew, K. Burke and M. Ernzerhof, *Phys. Rev. Lett.*, 1996, **77**, 3865–3868.
23 S. Grimme, *J. Comput. Chem.*, 2006, **27**, 1787–1799.
24 A. M. Rappe, K. M. Rabe, E. Kaxiras and J. D. Joannopoulos, *Phys. Rev. B*, 1990, **41**, 1227–1230.
25 N. Mounet and N. Marzari, *Phys. Rev. B - Condens. Matter Mater. Phys.*, 2005, **71**, 205214.
26 J. D. Pack and H. J. Monkhorst, *Phys. Rev. B*, 1977, 16, 1748–1749.
27 R. M. Wentzcovitch, *Phys. Rev. B*, 1991, **44**, 2358–2361.
28 M. Parrinello and A. Rahman, *J. Appl. Phys.*, 1981, **52**, 7182–7190.
29 M. Parrinello and A. Rahman, *Phys. Rev. Lett.*, 1980, **45**, 1196–1199.
30 W. Humphrey, A. Dalke and K. Schulten, *J. Mol. Graph.*, 1996, **14**, 33–38.
31 X. Ge, S. J. Binnie, D. Rocca, R. Gebauer and S. Baroni, *Comput. Phys. Commun.*, 2014, **185**, 2080–2089.
32 O. B. Malcioğlu, R. Gebauer, D. Rocca and S. Baroni, *Comput. Phys. Commun.*, 2011, **182**, 1744–1754.